Thermal Transport in Three-Dimensional Foam Architectures of Few-Layer Graphene and Ultrathin Graphite

Michael Thompson Pettes,[†] Hengxing Ji,[†] Rodney S. Ruoff,[†,‡] and Li Shi*,[†,‡]

[†]Department of Mechanical Engineering and [‡]Materials Science and Engineering Program, The University of Texas at Austin, Austin, Texas 78712, United States

Ⓢ *Supporting Information*

ABSTRACT: At a very low solid concentration of 0.45 ± 0.09 vol %, the room-temperature thermal conductivity (κ_{GF}) of freestanding graphene-based foams (GF), comprised of few-layer graphene (FLG) and ultrathin graphite (UG) synthesized through the use of methane chemical vapor deposition on reticulated nickel foams, was increased from 0.26 to 1.7 W m^{-1} K^{-1} after the etchant for the sacrificial nickel support was changed from an aggressive hydrochloric acid solution to a slow ammonium persulfate etchant. In addition, κ_{GF} showed a quadratic dependence on temperature between 11 and 75 K and peaked at about 150 K, where the solid thermal conductivity (κ_G) of the FLG and UG constituents reached about 1600 W m^{-1} K^{-1}, revealing the benefit of eliminating internal contact thermal resistance in the continuous GF structure.

KEYWORDS: *Graphene, graphite, foam, thermal conductivity, thermal management*
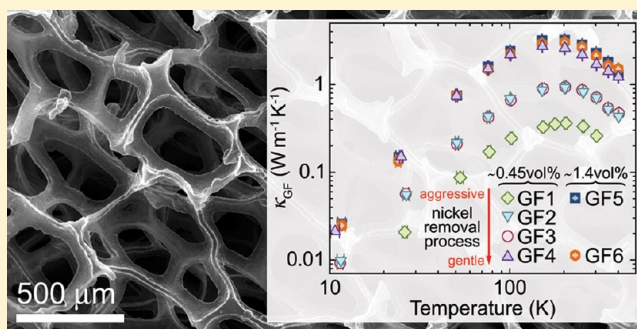
Owing to the very high thermal conductivity as well as the large surface-to-volume ratio for carbon nanotubes (CNTs)[1] and graphene,[2] these carbon nanomaterials have been investigated as nanofillers to enhance the thermal conductivity of lightweight polymeric composites,[3−7] as thermal interface materials in electronic packaging,[8−10] and as lateral heat spreaders to reduce the local hot spot temperature in nanoelectronic devices.[11,12] Among several factors including agglomeration, structural deformation, defects, and support or medium interaction[13,14] of the nanostructures, one critical issue that has prevented these CNT- and graphene-based networks to reach their full potential is the thermal contact resistance at their interface with both the medium and adjacent nanostructures.[15,16] In addition, the performance of thermal interface materials based on vertical CNT arrays has been limited by the small fraction of nanotubes making contact to both mating surfaces and the large interface thermal resistance between nanotubes in the array.[8−10] These problems can potentially be overcome by the recently reported macroscopic graphene-based foam (GF) structures[17] because internal contact thermal resistance may be greatly reduced or eliminated in these continuous, three-dimensional (3D) architectures of covalently bonded two-dimensional (2D) graphene building blocks. In fact, the reported room temperature electrical conductivity of polymeric composites with the graphene foam fillers is 1−6 orders of magnitude higher than those with individual CNT[4,18] or graphene[19] fillers at a similar volume loading fraction. However, thermal transport properties of the GF structures have not been reported.

In this Letter, we report temperature-dependent electron and phonon transport measurements of 3D GF structures consisting of few-layer graphene (FLG) and ultrathin graphite (UG) synthesized through the use of methane chemical vapor deposition (CVD) on open-celled reticulated nickel foam. Our measurement results show that the structure quality and transport properties of the freestanding GF with a solid concentration of ∼0.45 vol % depend much more sensitively on the etching process of the sacrificial Ni foam than on the grain size of the Ni foam. The room temperature effective thermal conductivity of the freestanding GF samples (κ_{GF}) with this very low solid concentration was increased 6.6 times after an aggressive Ni etchant was replaced with a gentle one. As the solid concentration was increased a factor of 3.1 by increasing the strut wall thickness, κ_{GF} was only increased a factor of 1.3, likely because of higher crystalline defects observed in the thicker strut walls. The obtained solid thermal conductivity, κ_G, for all samples can be explained by a theoretical model suggesting that κ_G is limited by phonon−phonon and phonon−boundary scatterings, instead of internal contact thermal resistance. Moreover, the theoretical analysis suggests an enhanced phonon−phonon scattering rate in GF and natural graphite (NG),[20] both of which contain internal folding, than in heat-treated highly oriented pyrolytic graphite (HT-HOPG).[21]

Six GF samples have been measured in this work, denoted as GF1−6. The GF was synthesized by saturation of carbon in

Table 1. Synthesis Conditions, Mass Density, and Room Temperature Effective and Solid Thermal Conductivity of Graphene-Based Foam (GF)

sample	Ni foam	growth time (h)	Ni etchant	$\rho_{m,GF}$ (10^{-3} g cm^{-3})	κ_{GF} (W m^{-1} K^{-1})	κ_{G} (W m^{-1} K^{-1})
GF1	as-purchased	1	HCl	10.0 ± 2.1	0.26	176 ± 37
GF2	as-purchased	1	Fe(NO$_3$)$_3$	9.6 ± 1.8	0.71	500 ± 95
GF3	annealed	1	Fe(NO$_3$)$_3$	9.9 ± 1.9	0.71	486 ± 93
GF4	annealed	1	(NH$_4$)$_2$S$_2$O$_8$	11.6 ± 1.9	1.70	995 ± 162
GF5	annealed	3	HCl	32.0 ± 2.7	2.28	484 ± 41
GF6	annealed	3	(NH$_4$)$_2$S$_2$O$_8$	31.7 ± 2.7	2.12	454 ± 38

reticulated Ni foam with a nominal pore size of ~590 μm at 1050 °C and precipitation of FLG or UG on its surface during cooling. Based on scanning electron microscopy (SEM) measurements, annealing the Ni foam at a temperature of 1100 °C before growth increased the grain size by ~2−3 times and created a noticeably smoother surface (Figure S1, Supporting Information). The Ni was subsequently removed using dilute HCl, Fe(NO$_3$)$_3$, or (NH$_4$)$_2$S$_2$O$_8$. The latter Ni etching processes based on ferric nitrate and ammonium persulfate were found to be much slower and gentler than that based on dilute hydrochloric acid, which caused bubble formation during the etching process. After the Ni support was etched away, the mass density ($\rho_{m,GF}$) and volume fraction (ϕ) for GF1−4 were 0.010±0.002 g cm^{-3} and 0.45±0.09 vol %, respectively, and were increased to 0.032±0.003 g cm^{-3} and 1.41±0.10 vol %, respectively for GF5,6 by increasing the growth time by a factor of 3. A summary of synthesis conditions, mass density, and corresponding room temperature thermal properties for each GF sample is given in Table 1. During the entire sample preparation processes, the GF samples were not exposed to polymer, which have been found to scatter electrons[22] and phonons[14] in graphene.

SEM analysis of the GF is shown in Figure 1. For the thin-walled lower volume fraction samples, GF1−4, the structure quality is seen to increase significantly as the Ni etchant is replaced from dilute HCl (GF1, Figure 1a) to the two slow etchants based on Fe(NO$_3$)$_3$ (GF2,3, Figure 1b,c) and (NH$_4$)$_2$S$_2$O$_8$ (GF4, Figure 1d). For the thick-walled higher volume fraction samples, GF5,6, the structure is noticeably more defective than GF1−4 regardless of the Ni etchant used (Figure 1e,f).
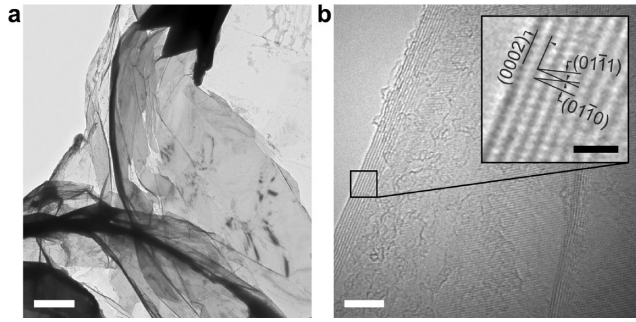
Phase contrast transmission electron microscopy (TEM) images of the freestanding GF samples are shown in Figure 2 and Figure S2 in the Supporting Information. Amorphous carbon was not observed in the TEM analysis, and stacking in the GF was directly observed to be AB ordered. X-ray diffraction (XRD) analysis of the GF is shown in Figure 3a, along with the reflection positions and intensities for SP-1 grade HOPG[23] for comparison. The {0002} interlayer spacing was measured to be 3.3679 Å, close to the 3.3553 Å reported for high-quality HOPG.[23] From the full width at half-maximum of the {0002} and {0004} reflections, we calculated the average thickness of the GF strut walls at ~14 nm, or ~40 layers, for GF1−4. On the basis of the same pore size and different mass densities, we estimated that the strut wall thickness was about 45 nm for GF5,6.

The GF strut wall was additionally characterized with micro-Raman spectroscopy at 488 nm laser excitation with an incident laser power on the order of a few milliwatts. The Raman spectra of the strut walls of the GF is shown in Figure 3b and matched well with those of high-quality graphite,[24] with the very low volume fraction GF1−4 showing no observable D peak and the
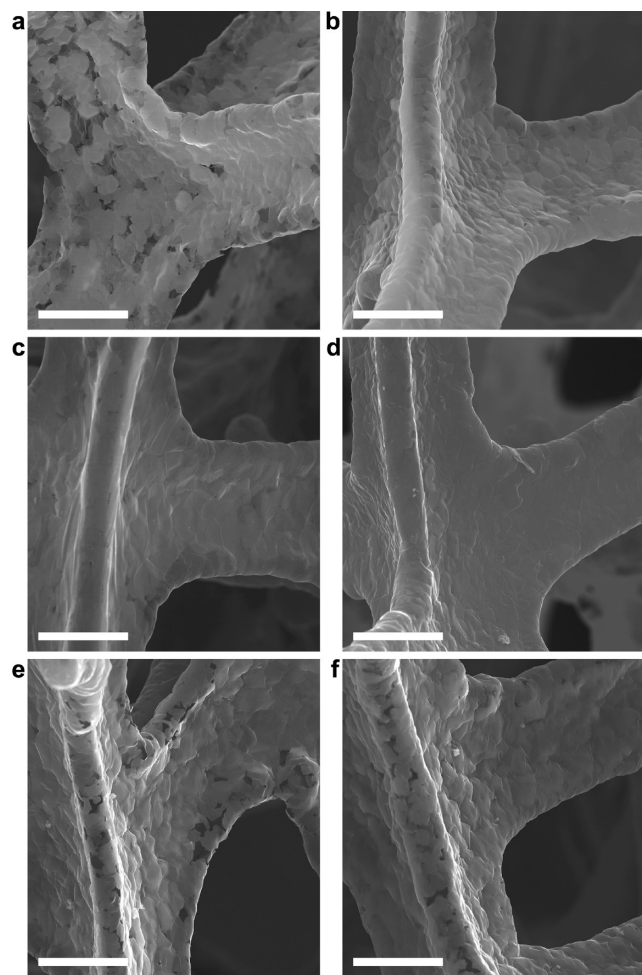

Figure 1. Scanning electron microscopy images of the strut walls of freestanding graphene-based foam (GF) samples (a) GF1, (b) GF2, (c) GF3, (d) GF4, (e) GF5, and (f) GF6. All scale bars are 50 μm.

thicker walled GF5,6 exhibiting a D peak to G peak intensity ratio of ~2%. The 2D peak to G peak intensity ratio for all samples was between 40% and 48%. Edges of voids present in the strut walls of GF1 also yielded characteristics of high-quality single- and few-layer graphene (Figure S3, Supporting Information), with small D peak to G peak intensity ratios of 1.6−3.3% likely resulting from edge states[25] instead of point defects within the FLG and UG. The GF was further characterized in the spectral width of interest for thermal radiation by Fourier transform infrared (FTIR) spectroscopy (Figure 3c).

The effective thermal conductivity of the GF, κ_{GF}, was obtained from the electrical resistance measured during electrical self-heating of the GF by a direct current. The thermal conductance of the GF is defined as $G_{GF} = \kappa_{GF}A/L$,

Figure 2. Transmission electron microscopy of GF1. (a) Low and (b) high resolution phase contrast micrographs near a void in the strut wall. (b, inset) Ordered AB stacking is observed at the folded edge of the 8-layer graphene, oriented close to the $[2\overline{1}\overline{1}0]$ zone axis, and measured interlayer spacing for the $\{0002\}$, $\{01\overline{1}1\}$, and $\{01\overline{1}0\}$ crystallographic planes closely match those determined more accurately through X-ray diffraction. Scale bars are 1 μm for (a), 5 nm for (b), and 1 nm for the inset in (b).
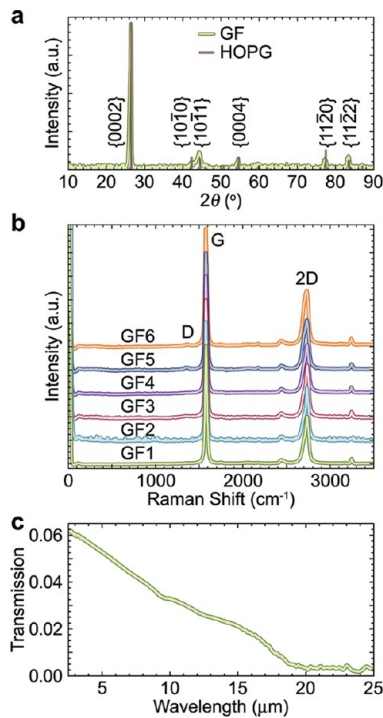
Figure 3. Optical characterization results. (a) X-ray diffraction spectrum of the GF shown in comparison with the reflection positions of SP-1 grade highly oriented pyrolytic graphite[23] (HOPG) normalized to the $\{0002\}$ reflection intensity. (b) Raman spectra of the six GF samples normalized to the G peak intensity. The main strut walls of GF1−4 exhibit spectra similar to defect-free bulk graphite[24] with no detectable D peak, while the thicker walled GF5,6 exhibit D peak to G peak intensity ratios of about 2%. (c) Fourier transform infrared (FTIR) spectrum normal to the ∼2 mm thick GF.

where $A = wt$ and w, t, and L are the width, thickness, and suspended length of the sample, respectively. As its dimensions were much larger than the nominal pore size within the foam, 590 μm, we can assume that the volumetric heat generation due to Joule heating, $\dot{q}$ is approximately uniform. We then account for heat transfer through both radiation and conduction with the following one-dimensional steady-state heat equation for the suspended GF[26]

$$\frac{\mathrm{d}}{\mathrm{d}x}\left(\kappa_{\mathrm{GF}}A\frac{\mathrm{d}T}{\mathrm{d}x}\right) - \frac{h_{\mathrm{r}}P(T - T_0)}{A} + \dot{q} = 0 \tag{1}$$

where $P = 2(w + t))$ and h_{r} is the effective radiation heat transfer coefficient.

We define the temperature rise along the length of the GF as $\theta(x) = T(x) - T_0$, where $x = 0$ is the midpoint and $x = \pm L/2$ are the end-points so that $\theta(x = 0) = \theta_{\mathrm{midpoint}}$ and $\theta(x = \pm L/2) = 0$. For small temperature rises, $\theta(x)$ much smaller than T_0, the effective radiation heat transfer coefficient reduces to

$$h_{\mathrm{r}} = 4\varepsilon_{\mathrm{GF}}(T_0)\sigma T_0^{\,3} \tag{2}$$

where $\varepsilon_{\mathrm{GF}}(T)$ is the emissivity and σ is the Stefan−Boltzmann constant. The $\varepsilon_{\mathrm{GF}}(T)$ calculated from the experimental FTIR result is shown in Figure S8 of the Supporting Information and is close to the upper limit of unity given for a black surface.

An analytical solution for G_{GF} can then be formed as

$$G_{\mathrm{GF}} = -\frac{\dot{Q}}{m^2 L^2 \overline{\theta}}\left[\frac{2}{mL}\tanh(mL/2) - 1\right] \tag{3}$$

where

$$m^2 \equiv \frac{h_{\mathrm{r}}P}{\kappa_{\mathrm{GF}}A} \tag{4}$$

and $\overline{\theta}$ is the average temperature rise of the electrically heated suspended GF. We additionally note that if we take the limit of eq 3 as $m \to 0$, i.e., the case where radiation heat transfer becomes negligible compared to conduction, the above solution can be reduced to the following simple form

$$\lim_{m \to 0} G_{\mathrm{GF}} = \frac{\dot{Q}}{12\overline{\theta}} \tag{5}$$

The obtained thermal conductance data of the GF samples is shown in Figure S9 of the Supporting Information and suggests that the radiation loss is not negligible for the low thermal conductance sample GF1 at temperatures above about 300 K and only causes a small error for this sample at lower temperatures and for the high conductance samples GF2−6 over the entire temperature range of measurements.

The total thermal conductivity of the GF is composed of both electronic and lattice contributions, $\kappa_{\mathrm{GF,e}}$ and $\kappa_{\mathrm{GF,l}}$, respectively. Using the Wiedemann−Franz law,[27] the electronic contribution to the thermal conductivity can be calculated from the electrical resistivity, ρ_{GF}, as $\kappa_{\mathrm{GF,e}} = LT/\rho_{\mathrm{GF}}$, where L is the Lorentz number and T is the temperature. Over the measured temperature range, the maximum value for $\kappa_{\mathrm{GF,e}}$ is only 0.2−3.6% of κ_{GF}. Hence, phonons make the dominant contribution to the thermal conductivity of the GF.

To determine the electrical and thermal properties of the FLG and UG constituents inside the GF, we use the approach of Lemlich[28] and Schuetz and Glicksman,[29] respectively. The solid electrical resistivity (ρ_{G}) and κ_{G} are then

$$\rho_{\mathrm{G}} = (\varphi/3)\rho_{\mathrm{GF}} \tag{6a}$$

and

$$\kappa_{\mathrm{G}} = (3/\varphi)\kappa_{\mathrm{GF}} \tag{6b}$$

Equations 6a and 6b have been reported to be accurate in describing electrical[30] and thermal[31] transport in open-celled metal foams at low φ. Although uncertainty remains in this model, subsequent semiempirical models do not deviate significantly from the these original expressions at low φ.[30,31]

However, the anisotropic thermal conductivity of the FLG and UG strut walls of the GF considered here may call for future studies to improve the model for GF.

Figure 4 shows the obtained effective and solid thermal conductivity and electrical resistivity values of the GF. The
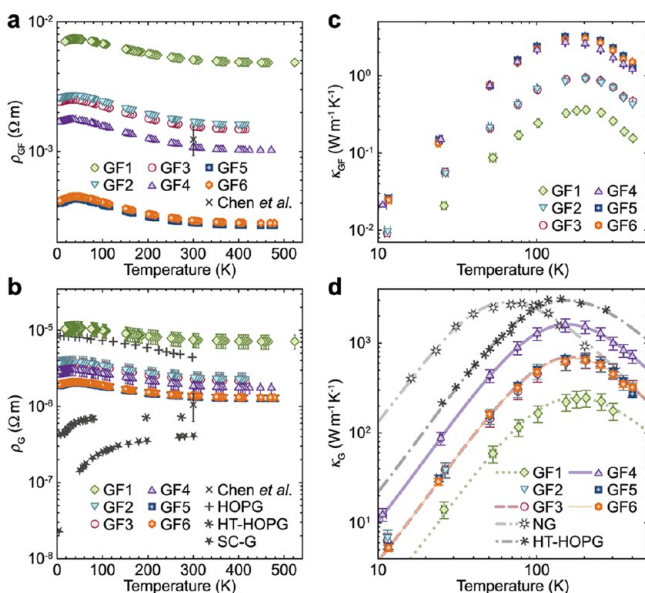
Figure 4. Temperature-dependent electrical and thermal properties. (a) Effective electrical resistivity of the GF (ρ_{GF}) shown in comparison with the range of values for GF reported by Chen et al.[17] (b) Solid electrical resistivity (ρ_G) of the few-layer graphene (FLG) and ultrathin graphite (UG) within the GF shown in comparison with the ρ_G of FLG in GF reported by Chen et al.,[17] highly oriented pyrolytic graphite deposited at 2250 °C (HOPG),[34] HOPG deposited at 2200 °C and subsequently heat treated to 3200 °C (HT-HOPG),[21] and single crystal graphite (SC-G).[35] (c) Measured effective thermal conductivity of the GF (κ_{GF}) and (d) solid thermal conductivity (κ_G) of FLG and UG within the GF. The κ of HT-HOPG[21] and natural graphite (NG)[20] are shown in comparison. The theoretical κ_G (lines) modeled according to eq 7 for the GF, HT-HOPG,[21] and NG[20] match the experimental values over a large temperature range.

~10−20% errors for these results were mainly due to the uncertainty in ϕ. The ρ_{GF} displayed a peak at a temperature near 40 K and decreased with increasing temperature above the peak position. A similar resistivity peak has been observed previously for HOPG,[32,33] although the exact mechanisms have not been understood clearly. Values of ρ_G for GF2,3 obtained with the gentle Fe(NO$_3$)$_3$-based Ni etch and GF4 obtained with the very slow (NH$_4$)$_2$S$_2$O$_8$-based Ni etch were a factor of 3 and 4 lower, respectively, than that for GF1 where the aggressive HCl-based Ni etch was used and a factor of 2 lower than that reported for HOPG deposited at 2250 °C.[34] Values of ρ_G for the higher density samples GF5,6 were 1.3 times lower than that for GF4. However, the ρ_G values for the GF were still higher than values reported for HT-HOPG[21] and single crystal graphite (SC-G)[35] likely because of the relatively low temperature used in GF synthesis. The ρ_{GF} and ρ_G for the GF structures reported by Chen et al.[17] are lower than the values of GF reported here, possibly because of unintentional doping of the GF by polymeric residue from the support layer used in that work.

For GF samples 1−3, 5, and 6, κ_{GF} reached a maximum at about 200 K, with a peak value ranging from 0.36 W m^{-1} K^{-1}

for GF1 to 0.92−0.94 W m^{-1} K^{-1} for GF2,3 among the low-density GF, and 3.0−3.2 W m^{-1} K^{-1} for the higher density GF5,6. The corresponding peak κ_G values were ~250 W m^{-1} K^{-1} for GF1 and ~650 W m^{-1} K^{-1} for GF2, 3 and GF5, 6. For sample GF4, with a low mass density and processed with the very slow ammonium persulfate-based Ni etching process, κ_{GF} reached a maximum at about 150 K with a peak value of 2.7 W m^{-1} K^{-1}, corresponding to a peak κ_G value of ~1600 W m^{-1} K^{-1}. Both the lower peak temperature and increased peak thermal conductivity are indicators of the increased crystalline quality of GF4. We note that although samples GF5,6 with thicker FLG/UG strut walls show lower ρ_G than the samples with thinner strut walls, the solid thermal conductivity of GF4 is higher than that for GF5,6. The lower solid κ_G of GF5,6 may be attributed to higher crystallographic defects consistent with SEM and Raman observations, which could be a result of thermal expansion mismatch between the Ni support and the precipitated graphitic layers and other factors, whereas the increased defects may possibly increase the charge carrier concentration and reduce the ρ_G of GF5,6.

It has been suggested that only well-oriented and well-annealed graphite exhibits a quadratic temperature dependence of the low-temperature thermal conductivity;[36] hence, the approximate $\kappa_G \propto T^2$ behavior observed for all GF samples between 11 and 77 K are indicative of well-oriented FLG and UG constituents. Additionally, the decreasing thermal conductivity with increasing temperature observed in the GF samples at $T > 200$ K reveals the dominant role of phonon−phonon scattering processes and suggests that the thermal conductivity is limited by phonon−phonon scattering and not internal contact thermal resistance. However, the κ_G values of the GF samples are still lower than the peak basal plane values reported for HT-HOPG[21] and NG,[20] where the peak also occurs at a lower temperature of about 140 and 80 K, respectively, as shown in Figure 4d.

We have analyzed the measurement results with the following thermal conductivity model[27]

$$\kappa = \sum_{p=1}^{12} \kappa_p$$

$$= \frac{1}{8\pi\delta k_B T^2} \sum_{p=1}^{12} \int_{k=0}^{k_{max}} \nu_p{}^2 (\hbar\omega_p)^2 \tau_p \frac{e^{\hbar\omega_p/k_B T}}{(e^{\hbar\omega_p/k_B T} - 1)^2} k\, dk$$

(7)

where δ is the {0002} interplanar spacing, k_B and $\hbar$ are the Boltzmann constant and the reduced Planck constant, respectively, τ_p is the relaxation time, ω_p is the phonon frequency, k is the wavevector, and ν_p is the phonon group velocity. The summation is over the 12 different phonon polarizations (p) of AB stacked graphite.[37] The crystallographic information obtained by XRD allows us to accurately determine δ and the Brillouin zone dimensions for the GF in addition to its AB stacked structure (Figure S9, Supporting Information).

In eq 7, the total polarization-specific relaxation time, τ_p, including contributions from phonon−boundary, phonon−impurity, and umklapp phonon−phonon scattering processes, is calculated using the relaxation time approximation (RTA) of Klemens and Pedraza.[38] Although it has been shown recently that the RTA does not adequately account for the selection rules governing phonon scattering in single- and few-layer graphene,[39] it can still provide important physical insights into thermal transport in graphite and the GF structures. For

example, by fitting the thermal conductivity data at low temperatures where boundary scattering is expected to be dominant, this model suggests that the phonon–boundary scattering mean free path is ~525 nm for GF1, 1.5 μm for GF2,3 and GF5,6, 4.25 μm for GF4, 9 μm for HT-HOPG,[21] and 55 μm for NG.[20] We note that the in-plane phonon mean free path is affected more strongly by lateral grain size and the interlayer coupling strength between the 2D graphene sheets in the FLG/UG strut walls, as opposed to scattering by the top and bottom surfaces of the strut wall, with the latter being the case for semiconductor thin films. The much smaller phonon–boundary mean free path value for GF1 than for GF2–6 is in agreement with the SEM observation of a high density of voids in GF1, presumably caused by the aggressive hydrochloric acid-based Ni etching process. However, the similar value found for GF2 and GF3 suggests that increasing the grain size of the sacrificial Ni foams did not noticeably reduce phonon–boundary scattering in the resulting GF3. The similar value found for GF5 and GF6 suggests that the structural integrity of the higher density GF, with correspondingly thicker strut walls, is much less sensitive to the Ni etching conditions than the low-density samples GF1–4. Moreover, the model suggests stronger phonon–phonon scattering in NG[20] and GF than in HT-HOPG,[21] approximately 6.3, 9.4, 3.9, and 1.1 times higher for NG,[20] GF1, GF2,3, and GF5,6, and GF4 at room temperature, respectively. According to a recent TEM study,[40] the grain size of the NG samples is larger than a millimeter, much larger than the 6–30 μm grain size for HOPG. Moreover, the TEM results reveal internal folded bands inside NG.[40] Similar folded bands can also be observed in the SEMs of our GF samples (Figure S1, Supporting Information). It remains to be investigated whether these folded bands may also lead to enhanced phonon–phonon scattering near the folded regions in addition to reducing the effective boundary scattering mean free path to be smaller than the grain size.

Despite the question on the effect of the folded bands, the continuous GF structure shows clearly superior thermal conductivity than other nanocarbon networks or metal foams. At a very low graphene loading of about 0.5 vol %, the effective room temperature thermal conductivity of 1.7 W m^{-1} K^{-1} of the GF is already a factor of 13–53, 2.6, and 8–12 higher than the filler contribution in polymeric composites with randomly oriented CNT,[3,4] magnetically aligned MWCNT,[4] and FLG/UG particle[5–7] fillers at similar loadings. Moreover, the GF samples with density 1.3–4.1 times lower than that of the sacrificial Ni foam can achieve a room temperature solid thermal conductivity that is a factor of 5–11 and 1.2–2.5 higher than for Ni and Cu, respectively.

Figure 5 shows an additional comparison between the effective thermal conductivity of GF samples in this work and pitch-derived carbon foams graphitized at 1000 and 2800 °C.[41] The mass density of the graphitized carbon foams is much larger than that for all the GF samples, mainly because of much thicker strut walls for the graphitized foams. Table S2 in the Supporting Information summarizes the specific thermal conductivity, defined as the ratio between the effective thermal conductivity and the mass density expressed in specific gravity. Both Figure 5 and Table S2 show that the specific thermal conductivity of the GF samples grown by CVD at a temperature of 1050 °C greatly exceeds that of the carbon foams graphitized at 1000 °C and approaches values reported for those graphitized at a much higher temperature of 2800 °C.
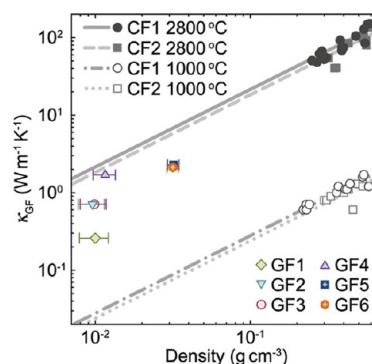
Figure 5. Comparison with graphitized carbon foams. Room temperature effective thermal conductivity of the GF (κ_{GF}) versus density shown in comparison with values reported for carbon foams derived from Mitsubishi ARA24 (CF1) and Conoco Dry Mesophase (CF2) pitches and graphitized at 1000 and 2800 °C.[41] Linear fits to the density dependence of the carbon foam thermal conductivity indicate the thermal conductivity of the GF, synthesized at 1050 °C, approaches the value expected for high-quality graphitic foam.

High-temperature annealing of the GF may lead to further enhancement of the specific thermal conductivity. Moreover, the GF structure with nanometer scale strut wall thickness can provide a much larger heat transfer surface area for a given solid volume than existing graphitic foams with micrometer scale strut wall thickness,[41] making GF more effective for heat transfer fin and filler applications based on the effective medium theory,[42] provided that the pore size of the GF can be reduced to achieve a comparable volume fraction as those of the graphitic foams without increasing the strut wall thickness.

These experiments lead to the establishment of the correlation between the transport properties of free-standing GF structures and the processing conditions. It is shown that enhancement in the thermal conductivity of the low-density GF by more than a factor of 6 can be obtained with the use of a slow etching process of the sacrificial Ni support. The thermal transport measurement results further reveal that phonon transport in the GF is only limited by the unfolded crystallite domain size at low temperature and phonon–phonon scattering near room temperature in the FLG/UG building blocks, as opposed to interface phonon transmission that has reduced the effective thermal conductivity of van der Waals-bonded carbon nanomaterial networks. Because the effective thermal conductivity is limited by the very low GF volume fraction instead of internal contact thermal resistance, it is feasible to further increase the effective thermal conductivity of this 3D graphene architecture by more than 1 order of magnitude via an increase in the graphene volume fraction through the reduction of the pore size without increasing the strut wall thickness. Therefore, this 3D graphene-based architecture holds great promise as thermal interface and heat spreading materials that meet the requirements in both the thermal conductivity and mechanical compliance for thermal management of electronic devices as well as thermal storage and electrochemical devices.[43]

■ ASSOCIATED CONTENT

Ⓢ Supporting Information

Additional SEM, TEM, and Raman analysis, synthesis and structural characterizations, thermal conductance measurement and analysis, theoretical thermal conductivity modeling, and

comparison with graphitized carbon foams. This material is available free of charge via the Internet at http://pubs.acs.org.

AUTHOR INFORMATION

Corresponding Author
*E-mail: lishi@mail.utexas.edu.

Notes
The authors declare no competing financial interest.

ACKNOWLEDGMENTS

REFERENCES

(1) Kim, P.; Shi, L.; Majumdar, A.; McEuen, P. L. *Phys. Rev. Lett.* **2001**, *87*, 215502−1−4.

(2) Balandin, A. A.; Ghosh, S.; Bao, W. Z.; Calizo, I.; Teweldebrhan, D.; Miao, F.; Lau, C. N. *Nano Lett.* **2008**, *8*, 902−907.

(3) Biercuk, M. J.; Llaguno, M. C.; Radosavljevic, M.; Hyun, J. K.; Johnson, A. T.; Fischer, J. E. *Appl. Phys. Lett.* **2002**, *80*, 2767−2769.

(4) Huang, H.; Liu, C. H.; Wu, Y.; Fan, S. S. *Adv. Mater.* **2005**, *17*, 1652−1656.

(5) Yu, A. P.; Ramesh, P.; Itkis, M. E.; Bekyarova, E.; Haddon, R. C. *J. Phys. Chem. C* **2007**, *111*, 7565−7569.

(6) Yavari, F.; Fard, H. R.; Pashayi, K.; Rafiee, M. A.; Zamiri, A.; Yu, Z. Z.; Ozisik, R.; Borca-Tasciuc, T.; Koratkar, N. *J. Phys. Chem. C* **2011**, *115*, 8753−8758.

(7) Shahil, K. M. F.; Balandin, A. A. *Nano Lett.* **2012**, *12*, 861−867.

(8) Xu, J.; Fisher, T. S. *Int. J. Heat Mass Transfer* **2006**, *49*, 1658−1666.

(9) Tong, T.; Zhao, Y.; Delzeit, L.; Kashani, A.; Meyyappan, M.; Majumdar, A. *IEEE Trans. Compon. Packaging Technol.* **2007**, *30*, 92−100.

(10) Panzer, M. A.; Zhang, G.; Mann, D.; Hu, X.; Pop, E.; Dai, H.; Goodson, K. E. *J. Heat Transfer* **2008**, *130*, 052401−1−9.

(11) Baloch, K. H.; Voskanian, N.; Cumings, J. *Appl. Phys. Lett.* **2010**, *97*, 063105−1−3.

(12) Yan, Z.; Liu, G.; Khan, J. M.; Balandin, A. A. *Nat. Commun.* **2011**, *3*, 827−1−−8.

(13) Seol, J. H.; Jo, I.; Moore, A. L.; Lindsay, L.; Aitken, Z. H.; Pettes, M. T.; Li, X.; Yao, Z.; Huang, R.; Broido, D.; Mingo, N.; Ruoff, R. S.; Shi, L. *Science* **2010**, *328*, 213−216.

(14) Pettes, M. T.; Jo, I.; Yao, Z.; Shi, L. *Nano Lett.* **2011**, *11*, 1195−1200.

(15) Prasher, R. S.; Hu, X. J.; Chalopin, Y.; Mingo, N.; Lofgreen, K.; Volz, S.; Cleri, F.; Keblinski, P. *Phys. Rev. Lett.* **2009**, *102*, 105901−1−4.

(16) Hu, L.; Desai, T.; Keblinski, P. *J. Appl. Phys.* **2011**, *110*, 033517−1−5.

(17) Chen, Z. P.; Ren, W. C.; Gao, L. B.; Liu, B. L.; Pei, S. F.; Cheng, H. M. *Nat. Mater.* **2011**, *10*, 424−428.

(18) Sandler, J.; Shaffer, M. S. P.; Prasse, T.; Bauhofer, W.; Schulte, K.; Windle, A. H. *Polymer* **1999**, *40*, 5967−5971.

(19) Stankovich, S.; Dikin, D. A.; Dommett, G. H. B.; Kohlhaas, K. M.; Zimney, E. J.; Stach, E. A.; Piner, R. D.; Nguyen, S. T.; Ruoff, R. S. *Nature* **2006**, *442*, 282−286.

(20) Smith, A. W. *Phys. Rev.* **1954**, *95*, 1095−1096.

(21) Bowman, J. C.; Krumhansl, J. A.; Meers, J. T. In *Industrial Carbon and Graphite*; Society of Chemical Industry: London, 1958; pp 52−59.

(22) Schedin, F.; Geim, A. K.; Morozov, S. V.; Hill, E. W.; Blake, P.; Katsnelson, M. I.; Novoselov, K. S. *Nat. Mater.* **2007**, *6*, 652−655.

(23) Howe, J. Y.; Jones, L. E.; Ow, H.; Rawn, C. J. *Powder Diffr.* **2003**, *18*, 150−154.

(24) Ferrari, A. C.; Meyer, J. C.; Scardaci, V.; Casiraghi, C.; Lazzeri, M.; Mauri, F.; Piscanec, S.; Jiang, D.; Novoselov, K. S.; Roth, S.; Geim, A. K. *Phys. Rev. Lett.* **2006**, *97*, 187401−1−4.

(25) Casiraghi, C.; Hartschuh, A.; Qian, H.; Piscanec, S.; Georgi, C.; Fasoli, A.; Novoselov, K. S.; Basko, D. M.; Ferrari, A. C. *Nano Lett.* **2009**, *9*, 1433−1441.

(26) Incropera, F. P.; DeWitt, D. P. *Fundamentals of Heat and Mass Transfer*, 5th ed.; J. Wiley: New York, 2002.

(27) Chen, G. *Nanoscale Energy Transport and Conversion: A Parallel Treatment of Electrons, Molecules, Phonons, and Photons*; Oxford University Press: New York, 2005.

(28) Lemlich, R. *J. Colloid Interface Sci.* **1978**, *64*, 107−110.

(29) Schuetz, M. A.; Glicksman, L. R. *J. Cell. Plast.* **1984**, *20*, 114−121.

(30) Goodall, R.; Weber, L.; Mortensen, A. *J. Appl. Phys.* **2006**, *100*, 044912−1−7.

(31) Krishnan, S.; Murthy, J. Y.; Garimella, S. V. *J. Heat Transfer* **2006**, *128*, 793−799.

(32) Reynolds, J. M.; Hemstreet, H. W.; Leinhardt, T. E. *Phys. Rev.* **1953**, *91*, 1152−1155.

(33) Klein, C. A.; Straub, W. D. *Phys. Rev.* **1961**, *123*, 1581−1583.

(34) Klein, C. *J. Appl. Phys.* **1962**, *33*, 3338−3357.

(35) Soule, D. E. *Phys. Rev.* **1958**, *112*, 698−707.

(36) Slack, G. A. *Phys. Rev.* **1962**, *127*, 694−701.

(37) Al-Jishi, R.; Dresselhaus, G. *Phys. Rev. B* **1982**, *26*, 4514−4522.

(38) Klemens, P. G.; Pedraza, D. F. *Carbon* **1994**, *32*, 735−741.

(39) Lindsay, L.; Broido, D. A.; Mingo, N. *Phys. Rev. B* **2011**, *83*, 235428−1−5.

(40) Park, S.; Floresca, H. C.; Suh, Y.; Kim, M. J. *Carbon* **2009**, *48*, 797−804.

(41) Klett, J.; Hardy, R.; Romine, E.; Walls, C.; Burchell, T. *Carbon* **2000**, *38*, 953−973.

(42) Nan, C. W.; Birringer, R.; Clarke, D. R.; Gleiter, H. *J. Appl. Phys.* **1997**, *81*, 6692−6699.

(43) Ji, H.; Zhang, L.; Pettes, M. T.; Li, H.; Chen, S.; Shi, L.; Piner, R.; Ruoff, R. S. *Nano Lett.* **2012**, *12*, 2446−2451.